International Journal of Hydrogen Energy 91 (2024) 1407–1421

Contents lists available at ScienceDirect

International Journal of Hydrogen Energy

journal homepage: www.elsevier.com/locate/he

R2Mx plant model for solar thermochemical hydrogen production at MW scale

Stefan Brendelberger

German Aerospace Center (DLR), Institute of Future Fuels, 51147 Cologne, Germany

ARTICLE INFO

Handling Editor: Prof B Shabani

Keywords:
Concentrated solar energy
Solar fuels
Thermochemistry
Ceria redox cycle
Receiver-reactor model

ABSTRACT

R2Mx is a new receiver-reactor concept for solar thermochemical water splitting cycles. The main difference to the current state-of-the-art is the use of a continuously operated reduction reactor with multiple mobile redox units. A plant model is developed for a version of the R2Mx concept with surrounding heliostat fields at MW scale. Performance estimates are derived over a large parameter space to characterize the plant and to identify possible technical challenges as well as research needs. Even without solid-solid heat recovery, the model predicts average annual plant efficiencies of up to 10.5% for multi MW receiver-reactors, which is comparable to commercial solutions. Furthermore, about 28% of the total energy input are energy losses occurring as highly concentrated radiation or as high temperature heat, emphasizing the improvement potential of the technology. Realizing the described enhancement options can turn this concept into an economic, large-scale fuel production technology.

Nomenclature

Symbols		Subscripts	
A	Area [m^2]	ap	Aperture
c	Specific heat capacity [J/(kg K)]	cav	Cavity
C	Concentration factor [−]	chem	Chemical
d	Thickness [m]	comp	Compensated
e	Emissivity [−]	conv	Convection
h	Molar enthalpy [J/mol]	eff	Effective
HHV	Higher heating value [J/mol]	el	Electrical
k	Thermal conductivity [W/(m K)]	ht	High temperature
M	Molar weight [kg/mol]	ins	Insulation
n	Number [−]; Amount [mol]	lt	Low temperature
p	Pressure [Pa]	opt	Optical
$\dot{q}$	Energy flow density [W/m^3]	ox	Oxidation
Q	Energy [J]	p	Constant pressure
$\dot{Q}$	Energy flow [W]	peri	Periphery
r	Radius [m]	prod	Product
R	Thermal resistivity [K/W]	rad	Radiation
t	Time [s]	rea	Reactor
T	Temperature [K]	rec	Receiver
Greek symbols		recov	Recovered
α	Free convective heat transfer coefficient [W/(m^2 K)]	red	Reduction
δ	Reduction extent [−]	sens	Sensible
ε	Efficiency [−]	shell	Receiver shell
η	Share; ratio; fraction; effectiveness [−]	sol	Solar
ρ	Density [kg/m^3]	spil	Spillage

(*continued on next column*)

(*continued*)

σ	Stefan-Boltzmann constant [W/(m^2 K^4)]	st	Solar thermal
Abbreviations		surf	Surface (receiver floor)
AEL	Alkaline electrolysis		
DNI	Direct normal irradiance		
PV	Photovoltaic		
R2Mx	Receiver-reactor cavity system with multiple mobile redox units		
RMA	Redox material assembly		
RPC	Reticulated porous ceramics		

1. Introduction

Deep decarbonization of several sectors, in particular transportation, will require the availability of renewable chemical energy carriers like hydrogen and other gaseous and liquid fuels at significant scale. One of the promising technological pathways under consideration for the large-scale production of economic renewable fuels are solar thermochemical redox cycles [1]. By making use of the full solar spectrum and by the direct conversion of high temperature heat into chemical energy, these cycles have a high theoretical efficiency potential, motivating the challenging undertaking of developing reactors and plants, that meet these expectations [2–4].

Amongst the redox cycles for solar thermochemical water splitting

E-mail address: stefan.brendelberger@dlr.de.

https://doi.org/10.1016/j.ijhydene.2024.10.050
Received 17 May 2024; Received in revised form 17 September 2024; Accepted 5 October 2024
Available online 23 October 2024

are two-step processes using a solid metal oxide and a temperature swing, pressure swing operation [5]. In a first step of the cycle, the metal oxide is reduced, with high temperatures and low partial pressures of oxygen promoting the progress of the reaction. In case of ceria as the metal oxide [6], the reduction reaction is non-stoichiometric and significant reduction extents, indicated by δ, require high temperatures (~1800 K) and low partial pressures (~100 Pa). In a second step, the reduced metal oxide is cooled to a temperature of around 1200 K and contacted with steam. During the resulting reaction the metal oxide is oxidized and hydrogen is produced as a fuel. The reactions of the ceria water splitting cycle are described in Equation (1) – endothermic reduction - and 2 – exothermic oxidation:

$$CeO_{2-\delta_{ox}} \rightarrow CeO_{2-\delta_{red}} + \frac{\Delta\delta}{2} O_2 \,, \tag{1}$$

$$CeO_{2-\delta_{red}} + \Delta\delta\, H_2O \rightarrow CeO_{2-\delta_{ox}} + \Delta\delta\, H_2, \tag{2}$$

with the cyclic change in reduction extent given as $\Delta\delta = \delta_{red} - \delta_{ox}$. The cycle can be also adopted to split CO_2 or for co-splitting of H_2O and CO_2.

Ceria is considered as reference material for the process due to fast kinetics and proven cyclic operation [7–11] but the development and characterization of other redox materials is an ongoing effort [12–21]. Furthermore, different design and operation choices are under assessment including the reaction temperatures [22–25] and pressures [26,27], the means of coupling the reactions to the solar interface [28,29], the means of removing released oxygen during the reduction reaction [30–35], and the physical form of the applied redox material [36–42]. Thus, different concepts for the technical implementation of the process are considered with a large variety of versions [43].

The receiver-reactor of the project SUN-to-LIQUID uses ceria in form of reticulated porous ceramics (RPC). It is operated in batch, and the two cyclic reactions are alternatingly realized in the same reactor [11,44–46]. The concentrated solar radiation is directed to the receiver-reactor only during the high temperature reduction step. After this, the receiver-reactor cools down without solar input and once the oxidation temperature is reached, the oxidizers are injected into the receiver-reactor. Heat losses are linked, amongst others, to the cyclic sensible heating of the redox material and inert parts of the receiver-reactor. A challenge of the concept is related to the direct exposure of the redox material to highly concentrated solar radiation and the relatively low thermal conductivity of the RPC. This leads to a highly inhomogeneous heating of the material, which is limiting the average reduction extent of the metal oxide significantly [47,48]. Experimentally demonstrated efficiencies for this receiver-reactor have been 4.1 % and 5.6 % for co-splitting and CO_2 splitting, respectively [11]. Due to the combination of power level, efficiency and in field demonstration the SUN-to-LIQUID technology can be considered as the state-of-the-art.

Several alternative approaches and concepts have been proposed but only a few have been experimentally tested [49–52]. Due to an increased complexity of the systems and resulting technical challenges, the state of development of these technologies falls behind the simpler, batch operated receiver-reactors described above. One of the alternative concepts at an early development stage is R2Mx (receiver-reactor cavity system with multiple mobile redox units) [53]. The system uses a continuously irradiated receiver-reactor cavity where the redox material of individually controllable redox material assemblies (RMA) is heated and reduced. From there, the redox material is moved vertically into separable oxidation reactors for the splitting step and afterwards back into the receiver-reactor cavity. In-between the reactors a solid-solid heat recovery system is foreseen to pre-heat the redox material on its way to the receiver-reactor. It is expected that the concept offers good part load performance and a promising scalability perspective.

Models of scaled receiver-reactors and of complete solar thermochemical fuel plants have been presented in literature. While scaled receiver-reactors using ceria have been simulated at higher levels of detail [54,55], plant models often only use simplified receiver-reactor representations with zero-dimensional descriptions of the redox structures based on thermodynamics [7,24,56–59] or even, in particular in the context of techno economic and life cycle assessments, consider the reactor efficiency as input parameter [60,61]. In case of R2Mx, a first numerical performance evaluation of a 250 kW receiver-reactor model has been presented previously [53]. On a plant level, the simulation of a receiver-reactor of type R2Mx has not been reported so far.

Here, a comprehensive model of a new version of the R2Mx water splitting plant with surrounding heliostat fields at MW scale is presented. The parametrized receiver-reactor model is based on the transient one-dimensional simulation of the redox structures. In a parametric study, 6 selected parameters are varied and the plant performance is evaluate using different metrics for 432,000 parameter sets. The main performance drivers are identified and opportunities for further improvements are described, along with the need for research and model refinement.

2. Method

2.1. Plant description - R2Mx with surrounding heliostat fields

The new version of R2Mx makes use of several apertures with secondary concentrators as in Ref. [53]. But in contrast to the mentioned study, here, the receiver-reactor is adapted to surrounding heliostat fields. The term surrounding field is chosen to highlight the more isotropic irradiation of the receiver-reactor as the heliostat fields provide concentrated solar radiation simultaneously to all apertures. Due to the limited acceptance angle of the secondary concentrator, the complete field will be divided into sub-fields [62,63]. By distributing the apertures over the circumference of the cylindrical receiver-reactor the radiative flux entering into the cavity is without a dominant direction. The ratio of total aperture area to cavity wall surface is small and presumably also the average view factors between redox structures and apertures. Furthermore, the evacuated receiver-reactor is continuously operated at temperatures well above 1700 K. Therefore, heat transfer to the redox material is expected to be dominated by thermal radiation from the hot surroundings within the cavity [55]. In order to better accustom to this indirectly heating cavity environment with a more isotropic flux distribution, the redox material is not applied as brick shaped redox structures like in Ref. [53], but as cylindrical bodies. The resulting difference in heating behavior will be analyzed by comparing an indirectly heated cylindric redox structure to a directly irradiated planar redox structure (see section 3.2). The latter one is an approximation for relatively thin redox structures covering the cavity walls of a receiver-reactor, as in the state-of-the-art technology [11]. A similar multi aperture cavity design was investigated by Groehn et al. [55] but with particles flowing through tubular absorbers made out of silicon carbide.

Fig. 1 shows a generic scheme of the complete plant comprising a receiver-reactor of type R2Mx. In the following the sub-systems of the R2Mx plant and the corresponding model assumptions and approximations will be described.

2.2. Details of sub-systems and approximations

2.2.1. Optical sub-system – surrounding heliostat fields and secondary concentrators

Heliostat fields are used commercially in concentrated solar power pants. Typically, concentration factors of about 500–1000 are achieved for receivers operating at temperatures below 1000 °C [64]. For solar thermochemical water splitting cycles much higher operating temperatures are necessary. In order to limit the relative radiative heat losses of a receiver-reactor, concentration factors beyond 2000 are targeted, which renders the application of secondary concentrators attractive. So

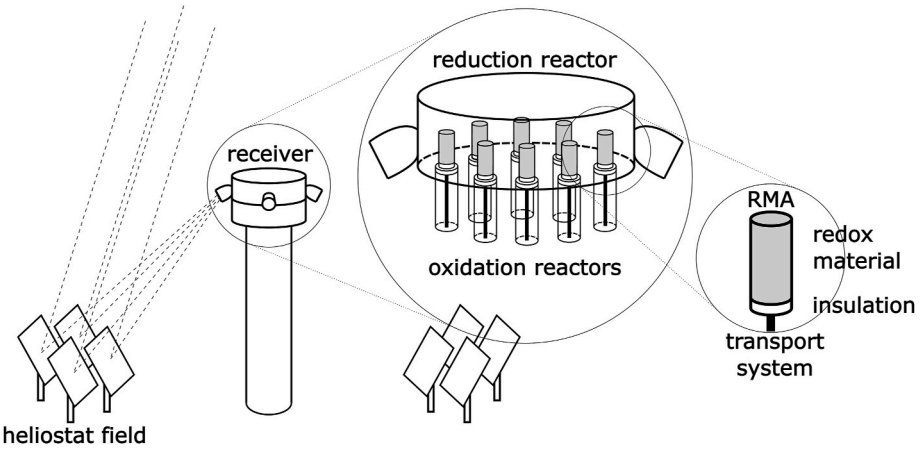

Fig. 1. Scheme of a solar thermochemical water splitting plant with a receiver-reactor of type R2Mx and surrounding heliostat fields. The receiver-reactor is shown as an enlarged section with cylindrical RMAs. The redox material is part of the RMA. To each RMA belongs a separate oxidation reactor underneath the reduction reactor and a vertical transport system.

far, in theoretical solar thermochemical fuel production studies the relationship between concentration factor and overall system performance was often neglected or the solar concentrator was put outside of the investigated system boundary [13,58]. In reality, solar concentrators tendentially show a decreasing optical efficiency with increasing concentration factor [65] for a fixed power at the outlet of the secondary. Martinek et al. [63] reported an increasing efficiency with concentration factor, which is suspected to be caused by a simultaneous reduction of the power level in the study. Therefore, on a plant level, a trade-off between optical efficiency and receiver-reactor efficiency is required. Since a detailed heliostat field design and optimization study is beyond the scope of this analysis, a linear relationship between optical efficiency and concentration factor is derived from relevant literature results presented by Pitz-Paal et al. [65].

2.2.2. *Solar receiver*

The receiver converts the concentrated radiation into high temperature heat which is processed in the reactor sub-system. In the following, these sub-systems are considered separately. The separation allows a similar description of the receiver as of solar thermal receivers which are used for the heating of a heat transfer medium. In the present case the quasi-continuous flow of redox material in and out of the receiver-reactor, realized by a large number of independently operated RMAs, approximates a continuous flow of an energy absorbing heat transfer medium through a receiver. This depicts a steady state description of the receiver reasonable. The interfaces between the sub-systems as well as the energy and mass flows are shown in Fig. 2 for the complete plant. The reactor comprises one reduction reactor cavity and one individual oxidation reactor for each RMA. The term receiver-reactor is used to describe the receiver with all reactor units.

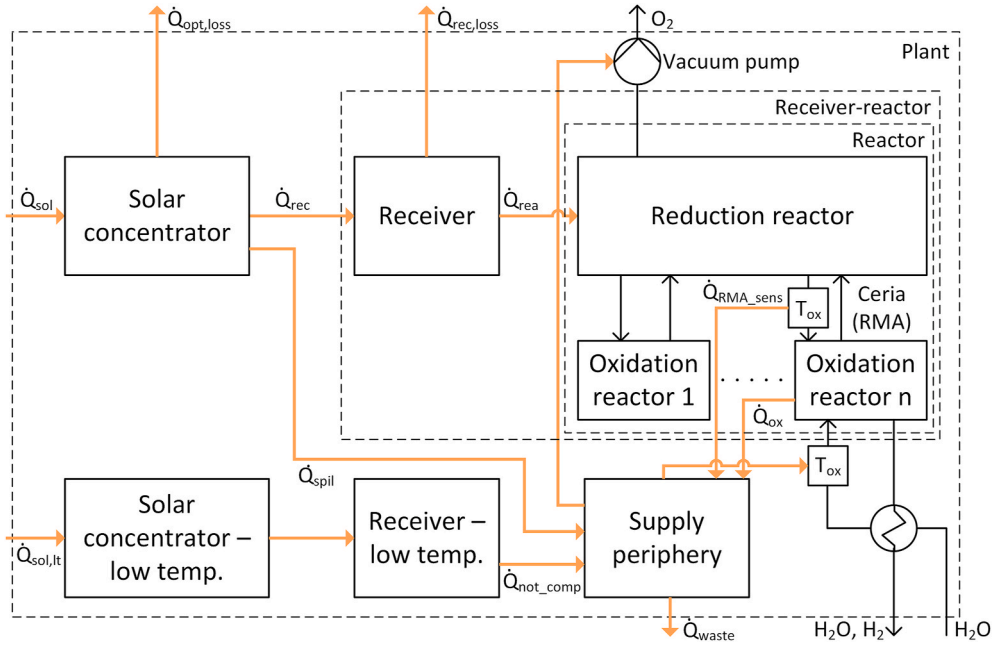

Fig. 2. Schematic of energy flows (orange arrows) and mass flows (black arrows). The interfaces of the different sub-systems are indicated by dashed lines. The dotted line in between "Oxidation reactor 1" and "Oxidation reactor n" indicates further oxidation reactors which are not depicted. The mass and energy flows of the oxidation reactors are shown as an example for the "Oxidation reactor n". (For interpretation of the references to colour in this figure legend, the reader is referred to the Web version of this article.)

2.2.3. Reactor

The reactor comprises the reduction reactor, the RMAs, and one oxidation reactor per RMA. These components are described in the following. The vertical transport systems and the gates separating the reaction atmospheres are also important and technically challenging parts of the reactor, but since they are less relevant for the plant performance analysis details will be published elsewhere.

2.2.4. Reduction reactor

In the cavity of the receiver-reactor the redox material is heated and reduced under an oxygen lean atmosphere, separated from the ambiance by windows. The required high temperature heat is provided by the receiver sub-system. The main simplifications of the reduction reactor model are.

- The change of state of one of the RMAs does not affect the other RMAs.
- All RMAs experience the same cavity environment with a uniform and constant temperature (T_{cav}).
- The transient energy and mass flows at the individual RMA level are averaged out at the reactor level enabling a steady-state description.

A uniform and constant cavity temperature is assumed to describe the heat losses of the receiver (radiation through the aperture and conduction through the insulated receiver walls) as well as the heat exchange by radiation with the redox material in the reduction reactor. In a real system some temporal and spatial fluctuation of the temperatures are unavoidable. Due to the high operation temperature of the receiver (well above 1700 K) and large open voids (the reduction reactor has intentionally a height 50% larger than the height of an RMA), filled with a mostly transparent oxygen atmosphere at low pressure, radiation will be the main means of heat transfer within the receiver-reactor and will lead to very effective heat exchange between sections at different temperatures. Numerical simulations of a cavity receiver operated at elevated temperatures with multiple tubular absorbers have shown, that local temperature differences are relatively small and that the temporal differences quickly even out despite of a highly non-uniform solar absorption [66]. Therefore, temperature differences are ignored as a first approximation and it is expected that a single effective cavity temperature is an important but reasonable simplification given the overall level of detail of the model.

2.2.5. Redox structure

In this study, the redox material is applied as a reticulated porous ceramic (RPC) in the shape of a cylinder. The properties of such ceria RPCs have been previously characterized and the correspondingly derived material models are implemented [48,67–69]. In order to simplify the modelling of the heat exchange between the redox structure and the reactor environment, the cylindrical RPCs is assumed to have an opaque outer shell, so that radiative heat transfer with the reactor is only considered in the outermost layer while radiation still contributes internally to heat transfer within the RPC. This is seen as a conservative approximation since it leads to a more inhomogeneous heating of the RPC, and as a consequence, to a lower reduction extent of the redox material in the center of the cylindrical body. Effects on top and bottom of the cylindrical redox structure are ignored and the RPC is spatially resolved only along its radius.

2.2.6. Oxidation reactors

For the oxidation reactor a generic representation is used. A homogeneous temperature at the end of the oxidation is assumed and its value is an input parameter to the model. Due to the relatively low oxidation temperature of 1200 K, almost full re-oxidation at moderate excess steam rates seems realistic assuming a quasi-counter flow pattern through connected oxidation reactors [70,71]. A steam conversion of 35% is assumed in combination with a reduction extent at the end of the oxidation of $\delta_{ox,end} = 0.001$ [72]. Despite the low level of detail, the oxidation reactor model is expected to provide reasonably accurate estimates of the energy flows. Modelling the oxidation reactor and its fluid streams in more detail is a complex task beyond the scope of this study.

2.2.7. Peripheral systems, heat recovery and parasitic energy demand

Peripheral systems considered in the plant model are the vacuum pumps and the components for provision of steam. The vacuum pumps are connected to the reduction reactor and they are assumed to operate at constant pumping speed, maintaining the oxygen atmosphere in the reduction reactor at a constant pressure while removing continuously the released oxygen. Since the considered vacuum pumps require electrical energy as input (see Table 1), a heat equivalent is determined to account for it in the energy balance of the plant.

It is envisioned that each redox structure has to be moved by less than a few meters per cycle. The estimated parasitic energy demand for the cyclic lifting of the redox material is more than two orders of magnitude smaller than the energy content of the produced hydrogen and is therefore not included in the model.

The energy for the provision of steam at the oxidation reactor temperature, starting from water at ambient temperature as a feed, is considered as additional parasitic heat demand. Separating hydrogen from unreacted steam without a gas-to-liquid transition is discussed in literature as an option to reduce the associated parasitic energy demand [73], but it is not considered here. The pressurization of the produced hydrogen is also not included in the model.

The R2Mx concept foresees the implementation of a solid-solid heat recovery system to transfer sensible heat from the hot redox material after the reduction to the cooler redox material after the oxidation. The heat recovery effectiveness of such a system strongly depends on many implementation details and its assessment is beyond the scope of this study. Therefore, a solid-solid heat recovery system is not included in the analysis but the model considers rather the generic use of recovered waste heat streams to compensate the parasitic energy demands. The concerned waste heat streams originate from the spillage of the concentrated solar radiation at the receiver, from the sensible heat of the redox material, from the exothermic reaction enthalpy during the oxidation and from the sensible heat of the product stream. For the recovery of sensible heat from the product stream, a gas-gas heat recovery effectiveness of 90% is assumed, while demonstrated values of up to 95% have been reported in literature [74]. For the other waste heat streams, no assumptions are made, how the heat integration is actually realized but it is expected, that the implementation of such a system is technically less challenging than an actual solid-solid heat recovery system. The applied waste heat recovery effectiveness of 30% is considered to be a rather conservative estimate.

The parasitic thermal energy demand that cannot be compensated by recovered waste heat is provided by a conventional concentrated solar thermal energy system. Since such a system can work at lower temperatures than the receiver-reactor for thermochemical water splitting, the respective solar concentrator and low temperature receiver are assumed with higher efficiencies compared to the one of the main plant (see Table 2).

2.3. Model implementation

The plant model was implemented in Python 3.11. In the following the main equations describing the sub-systems and the metrics for the evaluation of the plant will be provided.

2.3.1. Solar concentrator and receiver

The solar concentrator is modelled using linear relationships between the concentration factor, for values within a range of 2000–5000, and annual values of both, optical efficiency and share of spillage. The relationships have been derived from Pitz-Paal et al. [65]. The optical efficiency is described by

Table 1
Pump performance values (with $p_0 = 1\ Pa$) [75].

$Log_{10}(p/p_0)$ [–]	0	1.05	1.53	2.06	2.5	2.9	3.6	4.4	5
S / 10^3 $[m^3/h]$	44.3	56.3	59.1	55.3	49.6	23.6	7.1	3	2
P $[kW]$	70	75	81	102	148	111	85	76	70

Table 2
Fixed parameters.

Name	Symbol	Value	Unit	Source
Radial RMA discretization (number elements)		20	–	
Time discretization		1e-3	s	
Maximum duration of reduction		900	s	
Ambient temperature	T_{amb}	293.0	K	
Oxidation temperature	T_{ox}	1200.0	K	
Density of ceria	ρ	7220	kg/m^3	[48]
Molar weight of ceria	M_{CeO_2}	0.1721	kg/mol	[48]
Emissivity of ceria (at $T = 1773\ K$, $\delta = 0.038$)	e_{CeO_2}	0.62	–	[67]
Emissivity of receiver shell	e_{shell}	1	–	
Emissivity of aperture	e_{ap}	1	–	
RPC porosity		0.6583	–	[48]
Mean pore diameter		2.015	mm	[48]
Dual porosity		0.78	–	[48]
RMA height		0.5	m	
Gas constant		8.314	J/kg/K	
Stefan-Boltzmann constant	σ	5.67e-8	W/m^{2}K^4	
Extinction coefficient		435.24	1/m	[48]
Higher heating value (H_2)	HHV_{H_2}	286	kJ/mol	
Enthalpy of vaporization (H_2O)		40.6533	kJ/mol	[76]
Heat capacity of steam		38.39	J/mol K	[76]
Heat capacity of liquid water		75.3	J/mol K	[76]
Heat capacity of H_2 (at $T = 773\ K$)		29.38	J/mol K	[76]
Direct normal irradiation	DNI	1000.0	W/m^2	
Number apertures	n_{ap}	8	–	
Free convection heat transfer coefficient	α	10.0	W/m^{2}K	
Thermal conductivity insulation	k_{ins}	0.2	W/m K	
Receiver height		0.75	m	
Receiver radius		1.0	m	
Receiver shell surface	A_{shell}	17.7	m^2	
Insulation thickness	d_{ins}	0.2	m	
Reduction extent at end of oxidation	$\delta_{ox,end}$	0.001	–	[72]
Steam conversion		0.35	–	[72]
Conversion efficiency heat to electricity	$\varepsilon_{heat\_to\_el}$	0.4	–	[52]
Waste heat recovery effectiveness	η_{recov}	0.3	–	
Gas-gas heat recovery effectiveness		0.9	–	[74]
Solar thermal efficiency for low temperature heat	$\varepsilon_{st,lt}$	0.7	–	

$$\varepsilon_{opt} = -4.765{\cdot}10^{-5}{\cdot}C + 7.532{\cdot}10^{-1}, \tag{3}$$

with C being the concentration factor. Similarly, the share of spillage is given by

$$\eta_{spil} = 3.583{\cdot}10^{-5}{\cdot}C - 7.059{\cdot}10^{-2}. \tag{4}$$

The receiver geometry consists of a cylindrical metal housing with a layer of high temperature insulation. It has a number of circular apertures of equal size, distributed over its circumference. The power entering the receiver is given by

$$\dot{Q}_{rec} = \varepsilon_{opt}{\cdot}\dot{Q}_{sol} = n_{ap}{\cdot}A_{ap}{\cdot}C{\cdot}DNI. \tag{5}$$

With $\dot{Q}_{sol}$ being the solar radiative energy flow incident on the heliostat surfaces, the number of apertures n_{ap}, the area of a single aperture A_{ap}, the concentration factor C and the direct normal irradiance DNI. The thermal losses of the receiver $\dot{Q}_{rec,loss}$ are caused by thermal reradiation through the aperture $\dot{Q}_{ap,loss}$ and conductive heat losses through the insulated cylinder walls $\dot{Q}_{wall,loss}$.

$$\dot{Q}_{rec,loss} = \dot{Q}_{ap,loss} + \dot{Q}_{wall,loss}, \tag{6}$$

$$\dot{Q}_{ap,loss} = e_{ap} \cdot \sigma \cdot n_{ap} \cdot A_{ap} \cdot \left(T_{cav}{}^4 - T_{amb}{}^4\right), \tag{7}$$

$$\dot{Q}_{wall,loss} = \left(T_{cav} - T_{shell}\right) \ / \ R_{cond}, \tag{8}$$

with e_{ap} being the emissivity of the aperture and the Stefan-Boltzmann constant σ. The losses through the insulated receiver walls were calculated by solving a thermal resistance circuit with a conductive element in series with a parallel connection of a convection element and a radiative element representing the heat loss from the outer receiver shell to the ambiance. The resistivities are calculated as

$$R_{cond} = d_{ins} \ / \ (k_{ins} \cdot A_{shell}), \tag{9}$$

$$R_{conv} = 1 \ / \ (\alpha \cdot A_{shell}), \tag{10}$$

$$R_{rad} = 1 \ / \ \left(e_{shell}{\cdot}\sigma{\cdot}A_{shell} \cdot \left(T_{shell}{}^2 + T_{amb}{}^2\right) \cdot \left(T_{shell} + T_{amb}\right)\right), \tag{11}$$

with the thickness of the insulation d_{ins}, the thermal conductivity of the insulation k_{ins}, the convective heat transfer coefficient α, and the shell emissivity e_{shell}. The thermal energy flow provided to the reduction reactor is calculated as

$$\dot{Q}_{rea} = \dot{Q}_{rec} - \dot{Q}_{rec,loss} = n_{RMA}\frac{Q_{RMA}}{t_{red}}. \tag{12}$$

This flow of thermal energy heats and reduces a quasi-continuous flow of redox material through the receiver-reactor, generated by a large number of RMAs n_{RMA} cyclically entering and exiting the cavity. The net energy absorbed by an RMA Q_{RMA} , the reduction extent δ_{red} and the reduction duration t_{red} are results of the following transient simulation.

2.3.2. Transient heating of a single RMA

In order to calculate the net energy flow absorbed by an RMA in a cavity at constant temperature T_{cav} an unsteady one-dimensional heat transfer model is developed. The considered energy conservation equation is given by

$$\rho \cdot c_p \cdot \frac{\partial T}{\partial t} = \frac{1}{r} \cdot \frac{\partial}{\partial r}\left(r \cdot k_{eff} \cdot \frac{\partial T}{\partial r}\right) + \dot{q}_{chem}\ . \tag{13}$$

Convective contributions are neglected due to the low operating pressure. The finite volume method is applied and the discretized equations are solved using Euler-forward. The reduction step is simulated up to a maximum duration of 900 s. The effective thermal conductivity k_{eff} of the ceria RPC is modelled as function of temperature [68] which includes the contribution of radiation by the Rosseland diffusion approximation [50]. The heat capacity of ceria is given by [77]

$$c_p = \left(67.95\ K^{-1} - 9.9{\cdot}10^5\ K{\cdot}\ T^{-2} + 0.0125\ K^{-2}{\cdot}T\right) Jmol^{-1}/M_{CeO_2}, \tag{14}$$

with the molar mass of ceria M_{CeO_2}.The chemical source term $\dot{q}_{chem}$ is included in an effective heat capacity term as described in Refs. [78,79] by

$$\bar{c}_{eff} = \bar{c}_p - \frac{\Delta\bar{h}_{red}}{M_{CeO_2}} \frac{\partial\delta}{\partial T} . \quad (15)$$

With the change in enthalpy given by the fitted polynomial [69]

$$\Delta h_{red} = \left(478 - 1{,}158\,\delta + 1{,}790\,\delta^2 + 23{,}368\,\delta^3 - 64{,}929\,\delta^4\right) kJ mol^{-1}, \quad (16)$$

the average values of the heat capacity $\bar{c}_p$ and the reduction enthalpy $\Delta\bar{h}_{red}$ have been calculated using the respective temperature and delta dependent functions over the ranges defined by the oxidation temperature and the corresponding cavity temperature and reduction pressure. The temperature and partial pressure of oxygen p_{O_2} dependency of the reduction extent δ is implemented according to the thermodynamic model from Ref. [69], which is based on [80], with R being the molar gas constant.

$$\left(\frac{\delta}{0.35-\delta}\right) = 8{,}700 \left(\frac{p_{O_2}}{10^5}\right)^{-0.217} exp\left(\frac{\left(-195.6\ kJ\ mol^{-1}\right)}{R \cdot T}\right) . \quad (17)$$

Mass is conserved as an amount equal to all released oxygen per time step is assumed to be instantaneously removed by the vacuum pumps such that the partial pressure of oxygen is constant. The energy demand of the vacuum pumping system is calculated based on the scaled piecewise linear interpolation of the values power demand P and pump speed S from Ref. [75], based on [30].

The heat exchange by radiation at the surface of the RMA considers a cavity at constant temperature T_{cav}. At the beginning of each reduction step the RMAs are assumed to have a homogeneous temperature T_{ox} and a reduction extent δ corresponding to T_{ox} and p_{O_2}. These values are slightly below the assumed reduction extent at the end of the oxidation of $\delta_{ox,end} = 0.001$, leading to a conservative estimation of the required energy demand in the transient analysis.

The material models have been implemented previously in receiver-reactor models with RPC structures and where validated by comparison with experimental data [47,48]. A mesh study was conducted confirming a variation of the total reduction extent of below 0.5% compared to the converged solution. This was achieved for a radial discretization with 20 elements. Resultingly, the spatial resolution has a minimum of 0.5 mm and the time step width was set to a fixed value of 1e-3 s, respecting the stability criterion for the explicit scheme [81].

2.3.3. Number of RMAs and available space

The available surface area of the receiver which can be occupied by RMAs is limited due to geometrical considerations of the implemented design. The ratio between the maximum space available for RMAs to the floor surface area of the receiver is included in the model as a parameter called maximum surface fraction $\eta_{surf,max}$. For a fixed reduction duration, the power that can be processed by the reactor scales with the number of RMAs. Cases where the space of the RMAs necessary to process the power provided by the receiver is larger than given by $\eta_{surf,max}$ are discarded from further analysis.

2.3.4. Reduction duration

The unsteady heat transfer simulation of an individual RMA provides the evolution of the temperature and reduction extent distributions and therewith the net energy absorbed by an RMA Q_{RMA} as a function of the reduction duration t_{red}. As will be shown later (see Fig. 8), the net average power demand of a single RMA decreases monotonically with increasing reduction step duration. Furthermore, the reduction energy fraction η_{Q_red}, defined as the energy used for the reduction of the redox material compared to the total net energy absorbed by the redox material, is monotonically increasing with temperature for values within the investigated pressure and temperature range (see Fig. 3).

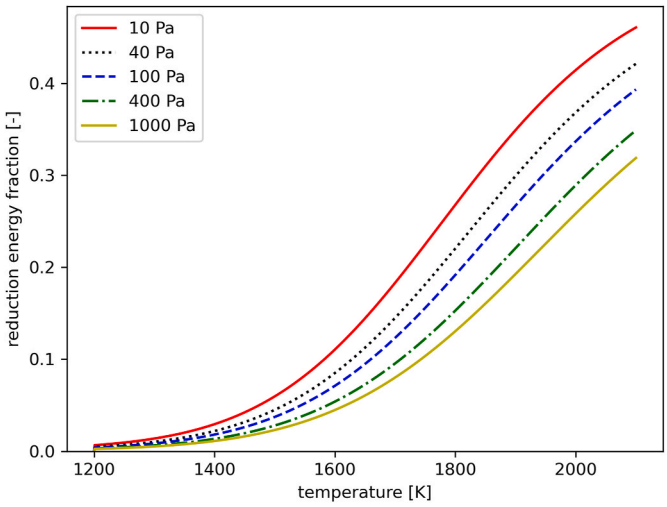

Fig. 3. The reduction energy fraction as function of temperature for different operating pressures based on ceria properties from Refs. [48,69].

$$\eta_{Q\_red}(T) = \frac{\frac{\Delta\bar{h}_{red}}{M_{CeO_2}}\left(\delta(T) - \delta_{T_{ox}}\right)}{\frac{\Delta\bar{h}_{red}}{M_{CeO_2}}\left(\delta(T) - \delta_{T_{ox}}\right) + \bar{c}_p\left(T - T_{ox}\right)} \quad (18)$$

Resultingly, the longer the reduction step duration, the more RMAs are necessary to process the thermal energy provided by the receiver. At the same time, longer reduction step durations increase the share of energy used for the reduction of the material, which is desirable from an efficiency perspective. Therefore, the number of RMAs should be chosen as high as possible. Consequently, for a given parameter set, the optimal reactor efficiency is obtained for the highest reduction duration which still respects the limit of the maximum surface fraction $\eta_{surf,max}$. The optimal reduction duration is accordingly derived. All other reduction durations are discarded from the parameter study.

2.3.5. Waste heat streams and parasitic energy demand

The recovered waste heat streams $\dot{Q}_{recov}$ are available for the compensation of the parasitic power demand of peripherical components $\dot{Q}_{peri}$. They are defined as:

$$\dot{Q}_{recov} = \eta_{recov}\left(\dot{Q}_{spil} + \dot{Q}_{RMA\_sens} + \dot{Q}_{ox}\right), \quad (19)$$

$$\dot{Q}_{spil} = \eta_{spil} \cdot \dot{Q}_{sol} = \eta_{spil} \cdot DNI \cdot A_{sol\_field}, \quad (20)$$

$$\dot{Q}_{RMA\_sens} = \sum_i \frac{m_{RMA,i}}{t_{red}} \bar{c}_P \cdot \left(T_{RMA,i} - T_{ox}\right) \cdot n_{RMA}, \quad (21)$$

$$\dot{Q}_{ox} = \sum_i \frac{m_{RMA,i} \cdot \Delta\bar{h}_R}{t_{red} \cdot M_{CeO_2}} \left(\delta_i - \delta_{ox}\right) - \dot{Q}_{H_2}, \quad (22)$$

$$\dot{Q}_{H_2} = 2 \cdot HHV_{H_2} \cdot \frac{n_{O_2}}{t_{red}} \cdot n_{RMA}, \quad (23)$$

with HHV_{H_2} being the higher heating value of hydrogen, n_{O_2} as the total amount of oxygen molecules released per RMA when reducing it from $\delta_{ox,end}$ to $\delta_{red,end}$, t_{red} being the duration of the reduction step and n_{RMA} as the number of RMAs applied simultaneously in the reduction reactor. Here it is to note, that n_{RMA} is not defined as an integer but as a real number, assuming that a shorter RMA would be used to account for the remainder.

The remaining thermal energy flow demand of the peripheral components after compensation is then calculated by:

$$\dot{Q}_{not\_comp} = \max\left(0, \dot{Q}_{peri} - \dot{Q}_{recov}\right) \quad (24)$$

The part of the waste heat stream that is not recovered is potentially attractive because it occurs as highly concentrated radiation or at high temperatures. It is given by:

$$\dot{Q}_{waste} = (1 - \eta_{recov}) \cdot \left(\dot{Q}_{spil} + \dot{Q}_{RMA\_sens} + \dot{Q}_{ox}\right) \tag{25}$$

2.4. Metrics

The most important metric is the average annual plant efficiency (also called plant efficiency), which covers all sub-systems from the solar collector to the produced hydrogen:

$$\varepsilon_{plant} = \frac{\dot{Q}_{H_2}}{\dot{Q}_{sol} + \frac{\dot{Q}_{not\_comp}}{\varepsilon_{st,lt}}} = \frac{\dot{Q}_{H_2}}{\dot{Q}_{sol} + \dot{Q}_{sol,lt}}, \tag{26}$$

with $\varepsilon_{st,lt}$ being the efficiency of the low temperature concentrated solar thermal system for the compensation of the remaining peripheral energy flow demand.

Another important metric is the receiver-reactor efficiency. It considers the radiative energy flow provided by the solar concentrator at the apertures as $\dot{Q}_{rec}$ and the equivalent heat flow demand of the vacuum pump, calculated with the heat-to-electricity conversion efficiency $\varepsilon_{heat\_to\_el}$. As no sweep gas is used, no related power demand has to be considered. For better comparison with the state-of-the-art results, the energy demand for the provision of steam is not included as in Refs. [10,11,46], while in general, it seems more consistent to include it [74,82].

$$\varepsilon_{rec\_rea} = \frac{\dot{Q}_{H_2}}{\dot{Q}_{rec} + \frac{\dot{Q}_{pump,el}}{\varepsilon_{heat\_to\_el}}} \tag{27}$$

The efficiency of the receiver is defined with the concentrated solar radiation at the apertures and the high temperature heat flow provided to the reduction reactor $\dot{Q}_{rea}$.

$$\varepsilon_{rec} = \frac{\dot{Q}_{rea}}{\dot{Q}_{rec}} \tag{28}$$

The solar thermal efficiency is the combined efficiency of the solar concentrator and the receiver.

$$\varepsilon_{st,ht} = \varepsilon_{opt} \cdot \varepsilon_{rec} = \frac{\dot{Q}_{rea}}{\dot{Q}_{sol}} \tag{29}$$

The subscript *ht* indicates that the operation temperature of the receiver is substantially higher than in the *lt* case of Equation (26). η_{waste} gives the share of the total energy input that is lost as highly concentrated radiation or as high temperature heat.

$$\eta_{waste} = \frac{\dot{Q}_{waste}}{\dot{Q}_{sol} + \dot{Q}_{sol,lt}} \tag{30}$$

In the chapter 3 also the resulting receiver inlet power, reduction step duration and number of RMAs are presented. For all parts of the model, energy and mass conservation were controlled and results were checked for consistency and plausibility.

2.5. Parameter space

One objective of this study is the evaluation of the performance metrics for a large number of parameter sets. A selection of 6 parameters has been varied in the parameter study while the rest of the parameters was kept constant. The constant parameters are given in Table 2. The parameters which have been varied are given in Table 3. The optimal reduction duration was directly derived (see section 2.4) reducing the number of investigated parameters sets by a factor of 900 (time step resolution 1 s, maximum reduction duration 900 s) to 432,000. For each of the varied parameters the investigated range is given as well as the value of the parameter set, that leads to the highest average annual plant efficiency of all the investigated sets, in the following also referred to as "peak efficiency set". The number of investigated values per parameter varies. For example, there are many more intermediate pointes in the range of investigated reduction pressures compared to the number of investigated cavity temperatures, since the latter shows an almost constant monotonic trend.

Table 3
Varied parameters.

Name	Symbol	Range	Unit	Number of values	Peak efficiency set
Cavity temperature	T_{cav}	1700.0–2100.0	K	5	2100.0 K
Reduction pressure	p_{O_2}	10.0–1000.0	Pa	18	105.0 Pa
RMA radius	r_{RMA}	0.01 - 0.05	m	5	0.01 m
Aperture radius	r_{ap}	0.06 - 0.33	m	10	0.18 m
Concentration factor	C	2000.0–5000.0	–	16	4400.0
Maximum surface fraction	$\eta_{surf,max}$	2.5–15.0	%	6	15.0 %

3. Results and discussion

In the following the results of the plant simulation are presented, starting with the analysis of the sub-systems solar concentrator and the receiver. The results dataset is available at [83].

3.1. Solar concentrator and receiver

The optical efficiency of the solar concentrator alone is not shown in a figure since this is just a linear dependency with values between 65.5 % at $C = 2000$ and 51.5 % at $C = 5000$ derived from two data points of a relevant study [65] as described in the methods section. More interesting is the performance of the receiver and the combination of the two systems, solar concentrator and receiver.

The varied parameters affecting the performance of the receiver are the concentration factor, the cavity temperature and the size of the apertures. Fig. 4 shows a contour plot of the receiver efficiency as a function of aperture radius and concentration factor. The other parameters correspond to the peak efficiency set. The efficiency increases monotonically with increasing concentration factor and aperture radius.

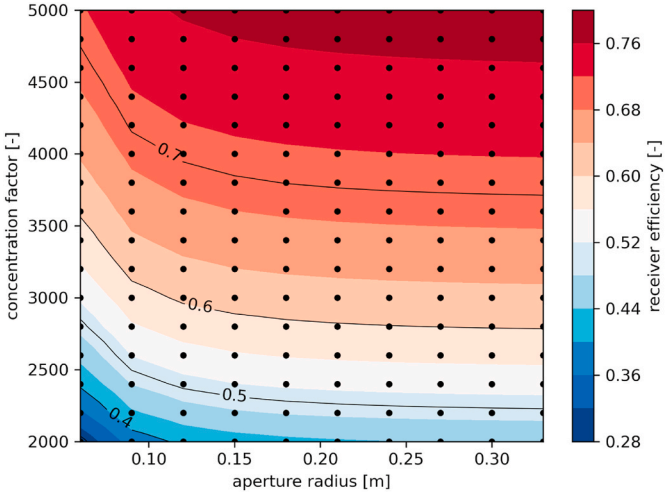

Fig. 4. Receiver efficiency as function of aperture radius and concentration factor. The black dots indicate the evaluated parameter sets while the contours are interpolated. The other parameters correspond to the peak efficiency set.

Since the conductive losses through the insulated walls of the receiver are not affected by the two parameters, they remain constant. Larger apertures lead to an inlet power increase and consequently smaller relative losses by conduction through the walls. Similarly, higher concentration factors lead to smaller relative radiative losses for a receiver operated at a fixed temperature (cavity temperature).

While high concentration factors are in general favorable for the receiver efficiency, it is the opposite for the solar concentrator. This trade-off can be seen if the combination of solar concentrator and receiver as in Fig. 5. Higher cavity temperatures are related to higher heat losses at the receiver and have therefore a negative effect on the receiver efficiency. The benefit of higher cavity temperatures will only become apparent once the reactor is included in the analysis, as shown below.

The total concentrated solar radiation input at the apertures of the receiver is defined by the total aperture size, the concentration factor and the DNI (see Equation (5)). It scales linearly with the concentration factor and quadratic with the aperture radius. Since the number of apertures is kept fixed in this study the total aperture size changes only with the aperture radius.

Fig. 6 provides an overview of the receiver input power for the investigated parameter ranges. As can be seen, the investigated plants have receiver input powers of up to 13.7 MW. The plant with the highest efficiency has a receiver input power of 3.7 MW and a solar field input power of 7.0 MW. While it is typically assumed that a single aperture will be limited in size by the availability of appropriate commercial windows, the system cloud be scaled by increasing the number of apertures as well as the size of the receiver-reactor and the number of RMAs.

3.2. Heating and reduction of a cylindrical redox structure

Central to the evaluation of the reactor performance is the simulation of the redox material after entering the receiver-reactor cavity. As described above, it is assumed that the redox material with cylindrical geometry is exposed to an environment at uniform and constant temperature (cavity temperature) and constant partial pressure of oxygen (reduction pressure). After entering the cavity, the redox material temperature converges to the cavity temperature. The temperature gradient over the radius of the RMA decreases with time after an initial steep increase.

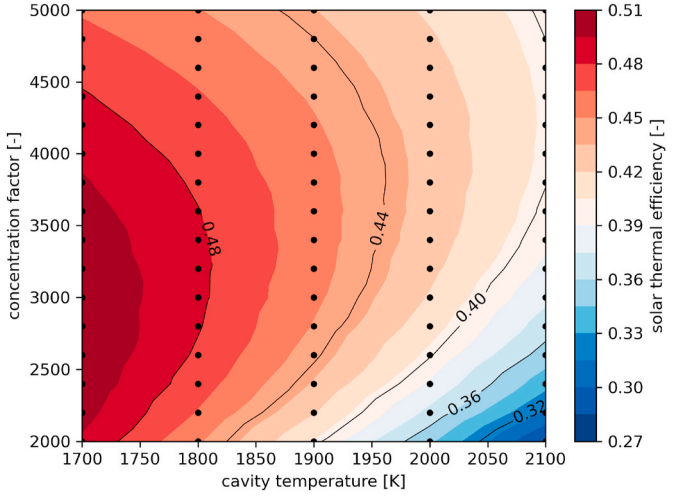

Fig. 5. The solar thermal efficiency is obtained as the efficiency product of solar concentrator (optical) and receiver and is displayed as function of cavity temperature and concenctration factor. The other parameters correspond to the peak efficiency set.

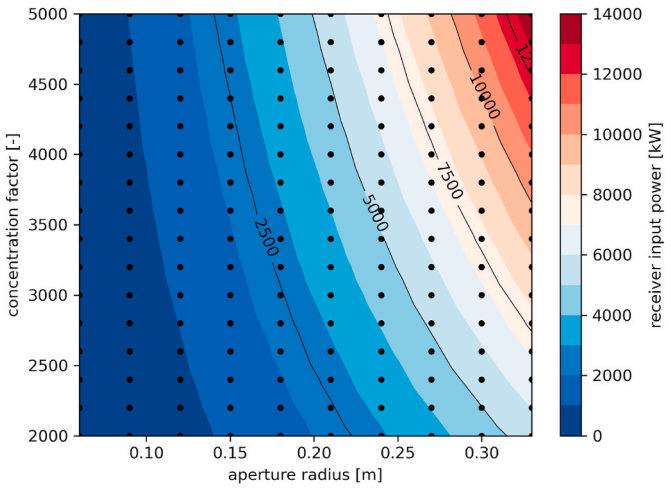

Fig. 6. Input power by concentrated solar radiation to the receiver as function of aperture radius and concentration factor.

3.2.1. Comparison of heating pattern with simplified state-of-the-art receiver-reactor model

It is interesting to compare the resulting heating pattern of the redox material to the one obtained in a state-of-the-art receiver-reactor [11]. For this comparison a simplified directly irradiate state-of-the-art receiver-reactor was modelled using also a transient one-dimensional heat transfer description and the same material models (see Equations (13)–(17)). In the state-of-the-art case the lateral dimensions of the redox material are typically much larger than the dimension perpendicular to the irradiated surface (compare to Ref. [47]). Thus, the redox material in this case is described as a plate irradiated from one side. It is discretized perpendicular to the directly irradiated surface applying the material properties of an RPC as described above.

The concentration factor in the state-of-the-art case is set to 2500, the aperture radius to 0.08 m, and the RPC thickness to 0.035 m [11,48]. The cavity walls are considered adiabatic to omit corresponding heat losses for the comparison study. The RPC radius for the cylindrical case is set to 0.035 m, so that the maximum distance from the heated surface to the interior is the same in both cases. The height of the cylinder and the cavity temperature are chosen to obtain in both cases the same total mass (20 kg) and the same total absorbed energy (9.24 MJ) after 360 s. This leads to a cavity temperature of 1915 K.

For the illustration of the comparison the temperature-dependent mass fraction distributions are derived. Fig. 7 shows the resulting distributions for three points in time during the reduction step, displaying substantial qualitative and quantitative differences. The top of Fig. 7 shows the distribution in case of the state-of-the-art (direct, plate) and the bottom of Fig. 7 the one in the R2Mx case (indirect, cylinder). After 120 s the temperature spread is considerably larger in case of the plate (456 K vs. 192 K) and most of the material has a temperature at the lower end of the distribution while in case of the cylinder the highest mass fraction values are reached at the highest temperatures. This difference is qualitatively maintained over the whole investigated reduction duration. The temperature spread in case of R2Mx is decreasing with time to a spread of 17 K at the end of the period while the spread in case of the plate is still about 184 K wide. This indicates that the heating of a cylindrical redox material in a constant temperature cavity leads to a much more benign temperature distribution than the heating in the state-of-the-art case. One can anticipate a notable positive impact on the reduction reactor efficiency as a result.

Another significant consequence of the different heating environments is related to the maximum temperature. In the indirectly heated R2Mx case, the redox material temperature is converging towards the constant cavity temperature (here 1915 K) while in the state-of-the-art

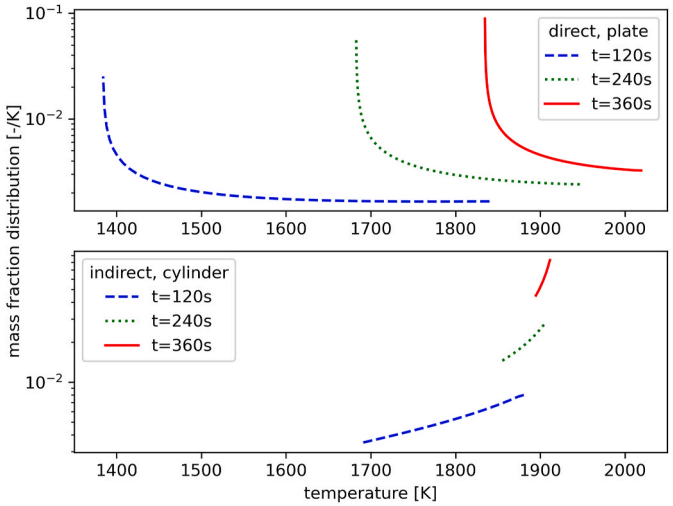

Fig. 7. Temperature-dependent mass fraction distribution for different reduction times. Top: directly irradiated plate shaped redox structure (state-of-the-art); Bottom: indirectly heated cylindrical redox structure (R2Mx).

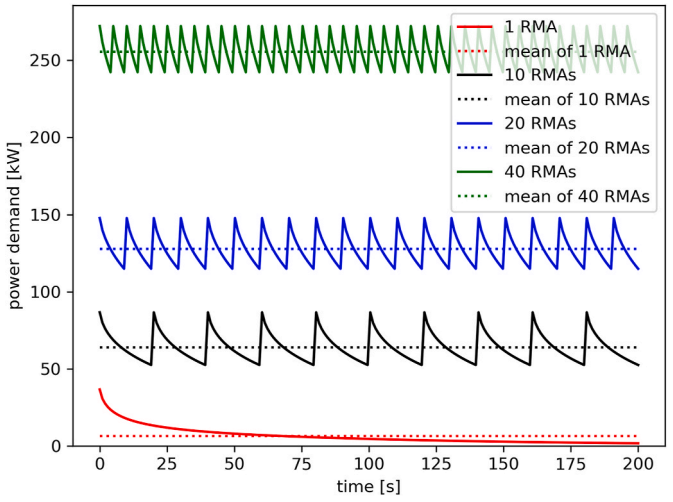

Fig. 8. Reduction reactor power demand as a function of time for systems applying different numbers of RMAs ($T_{cav} = 1915\,K$, $r_{RMA} = 0.035\,m$, $t_{red} = 200\,s$).

case the redox material is approaching an equilibrium temperature, at which the heat losses match the radiation input. In the given example with a concentration factor of 2500, the equilibrium temperature is 2575 K. As these temperatures pose a significant risk of material failure, the reduction step is typically stopped well in advance, resulting in large temperature gradients. On the other side, operating at lower concentration factors increases the relative re-radiation heat losses and consequently decreases the system efficiency. For example, Thanda et al. [82] applied relatively small concentration factors (peak flux below 1.5 MW/m^2) and reported comparably low efficiency values for a receiver-reactor system. Alternatively, a decrease of the solar power input with time was proposed [84]. The system efficiency benefits from such a strategy only if the solar resource, that becomes available, is exploited in parallel elsewhere [75,85].

In the indirect heating case the cavity temperature is the theoretical upper temperature for the redox material during operation. In a real system, it is rather an effective temperature value and somewhat higher temperatures are to be expected, but the effective radiative heat transfer will tend to even out temperature deviations quickly (see section 2.2). The cavity temperature can not only be tailored by design choices but also be controlled during operation, amongst others, by adapting the process step durations, the number of RMAs operated simultaneously, the reduction pressure, or the applied solar concentration.

3.3. Reduction reactor with multiple RMAs

After this general description of the heating of single RMAs, and the insertion of a comparison with a state-of-the art receiver-reactor, the performance of a reactor applying a large number of RMAs simultaneously is analyzed. The energy flow absorbed by the RMAs defines the thermal power demand of the reduction reactor. At each point in time there are several RMAs in the reactor and one after the other moves in and out at the start and at the end of its respective individual reduction step. The result is a smoothening of the power demand and in the limit, with a large enough number of RMAs, an almost constant value for the power demand with small relative fluctuations. Exemplary, the power demand profile of a receiver reactor with 1, 10, 20 and 40 RMAs and a reduction duration of 200 s is presented in Fig. 8.

The curves were obtained by adding up shifted power demands of single RMAs (see section 3.2) with an assumed RMA height of 0.5 m and a radius of 0.035 m. The relative amplitude of the power demand fluctuations is decreasing and their frequency increasing with increasing number of RMAs. As shown below the number of RMAs derived for the investigated parameter sets is typically well above 40 (see Fig. 15). Considering in addition the thermal inertia of the system a constant power demand appears to be a reasonable approximation.

3.4. Receiver-reactor

Assessing the combination of the sub-systems, receiver and reactor (reduction reactor and oxidation reactors), helps to put the performance in perspective with reported performance values of systems presented in literature [10,11,82]. The resulting receiver-reactor efficiency, in literature often named “solar-to-fuel efficiency” or similar, is shown in Fig. 9 as function of the RMA radius and of the concentration factor, with the other parameters fixed at the peak efficiency set (see Table 3).

The receiver-reactor efficiency maximum is observed at the upper limit of the concentration factor range. At low concentration factors, the radiative heat losses become dominant reducing the receiver-reactor efficiency. The peak values of around 17.6% of the R2Mx model for the parameters shown in Fig. 9 are significantly above experimentally demonstrated values for the state-of-the-art technology of 5.6% (for CO_2-splitting), illustrating the promising performance potential of

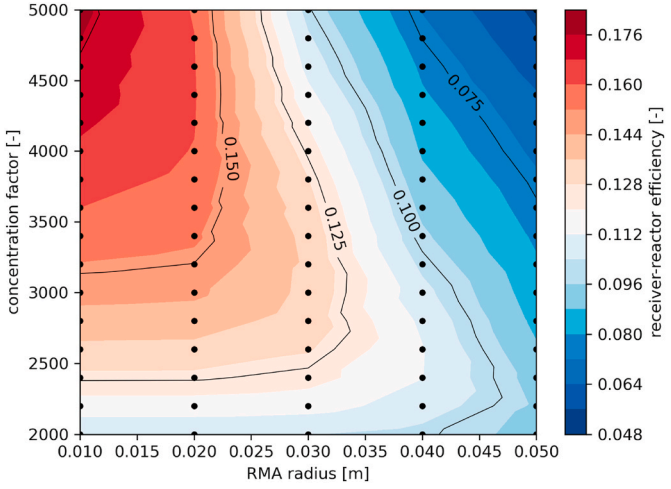

Fig. 9. Receiver-reactor efficiency as function of the RMA radius and of the concentration factor. A maximum value of around 17.6% is obtained at the upper limit of the investigated concentration factor range and the lower limit of the RMA radius range. The other parameters are fixed to the peak efficiency set.

R2Mx. This impression is further strenghened when looking at the overall plant performance.

3.5. Plant performance

After analyzing the sub-systems solar concentrator, receiver, reactor and their combinations the overall plant performance is assessed, from the concentration of solar radiation until the production of hydrogen. In contrast to the efficiency metrics used above, the plant efficiency (Equation (26)) considers the use of recovered waste heat to compensated parasitic demands for the vacuum pump and for the steam provision system (heating of H_2O from ambient temperature to the oxidation temperature including vaporization). The maximum annual average plant efficiency obtained in the parameter study is 10.5 %, which is close to the expected annual efficiency of 11 % for commercial photovoltaics (PV) coupled to alkaline electrolysis (AEL) [86].

First, the plant performance is evaluated varying only one parameter at a time while all other parameters are chosen to obtain the highest plant efficiency. This represents a projection of the highest plant efficiency values onto the one dimension given by the respective parameter. The resulting plant efficiencies are shown in Fig. 10 (left) for normalized versions of the parameters P_{norm} using:

$$P_{norm} = (P - P_{min}) / (P_{max} - P_{min}) \quad (31)$$

The sensitivity of the plant efficiency is relatively large with respect to the cavity temperature, reduction pressure and concentration factor. Smaller sensitivities can be identified for the RMA radius, the aperture radius and the maximum surface fraction. The linearly interpolated efficiencies show a monotonic behavior for the cavity temperature, the RMA radius and the maximum surface fraction. Peak values within the parameter range can be identified for the concentration factor, the aperture radius and, most pronounced, for the reduction pressure. Based on the efficiency values presented in Fig. 10 the receiver-reactor cavity should be operated at temperatures as high as possible. This finding seems a bit surprising given that it was derived for a system not employing any solid-solid heat recovery, but already Fig. 3 indicates, that heat recovery is actually more important at lower reduction temperatures. The optimal operation temperature is accordingly defined by material stability limitations rather than efficiency considerations. Similarly, the partial pressure of oxygen has a large effect on the overall performance, and in particular too small values seem prohibitive. Since low partial pressures of oxygen require large vacuum pumping systems, also from a technical implementation and a cost perspective the vacuum pumping system will have to be limited in size.

Another important metric is the waste fraction (see Equation (30)) depicted in Fig. 10 (right) since it quantifies the unused high-quality energy losses. For the same parameter sets as in Fig. 10 (left), values mainly between 25% and 30% can be identified. This shows that these high-quality waste streams make up a large fraction of the total energy input which could to be further exploited. In case of the peak performance set, the waste fraction is 28%.

After the assessment of the impact of single parameters on the plant efficiency, combinations of two parameters are analyzed in more detail. Similar to the methodology applied for Fig. 10 the parameters which are not shown in the figure are selected to provide the highest plant efficiency. Consequently, the other “free” parameters might change in the figure from one data point (black dots) to the next. This approach allows to better assess the performance potential of the plant with respect to sets of two parameters at a time.

In Fig. 11 the concentration factor as well as the reduction pressure are varied as indicated by the two axes. The highest plant efficiencies are obtained at relatively low reduction pressures (maximum at 105 Pa) and high concentration factors (maximum at 4400). The plant efficiency is particularly sensitive to changes in reduction pressure at values below 200 Pa. This sensitivity is less pronounced at lower concentration factors.

Similarly, the effect of reduction pressure and cavity temperature on the plant performance can be assessed (see Fig. 12). As already indicated in Fig. 11, reducing the reduction pressure until approximately 100 Pa improves the plant efficiency. Lowering the reduction pressure beyond this point has a negative effect due to a strong increase of parasitic energy demand for the vacuum pump, which cannot be compensated by recovered waste heat streams anymore. In this low-pressure area, the plant efficiency maximum is shifting towards lower pressures for lower cavity temperatures. One reason for this is expected to be the smaller amount of oxygen released at lower temperatures and the resulting lower vacuum pumping parasitics in these cases.

In agreement with Fig. 10 the plant efficiency in Fig. 12 favors high

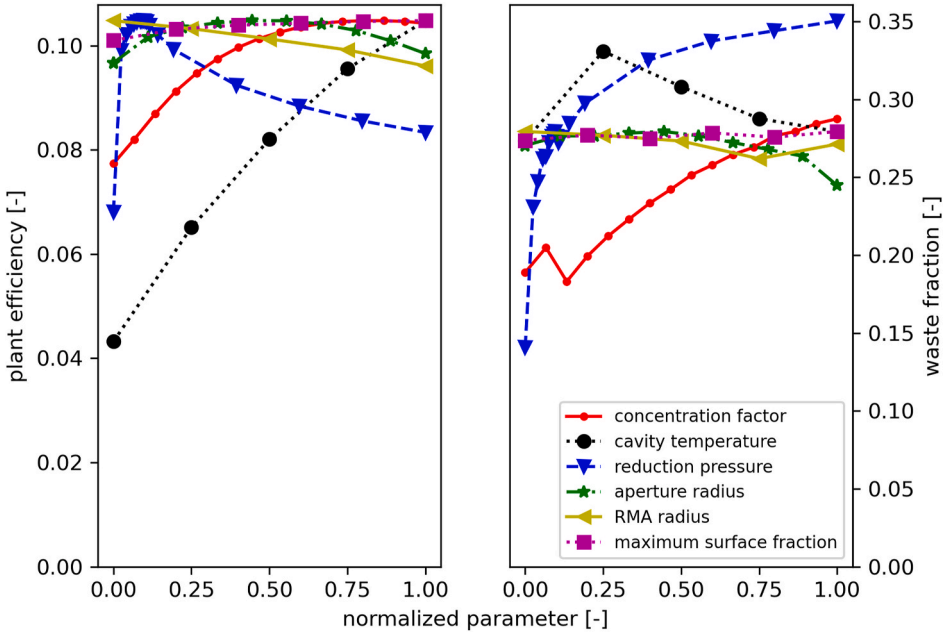

Fig. 10. Left: Plant efficiency as function of the normalized parameters. For a given normalized parameter, the plant efficiency value shown is the highest value in the analyzed parameter set; Right: For the same parameter sets as in the left figure, the waste fraction is depicted.

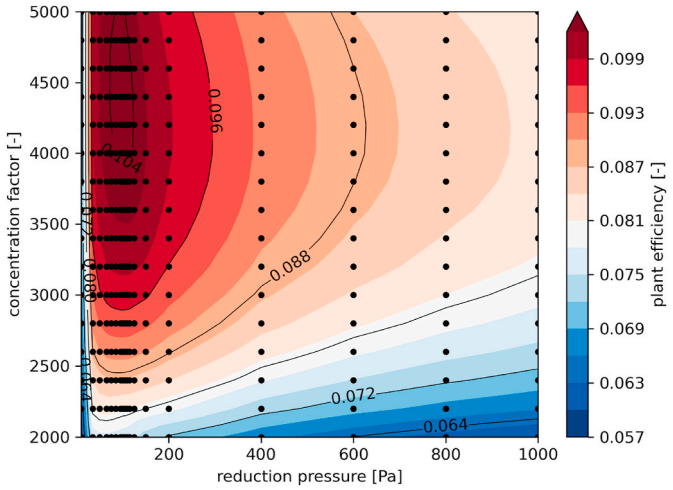

Fig. 11. Plant efficiency as function or reduction pressure and concentration factor. The other four "free" parameters are selected individually at each data point such that the plant efficiency is optimized.

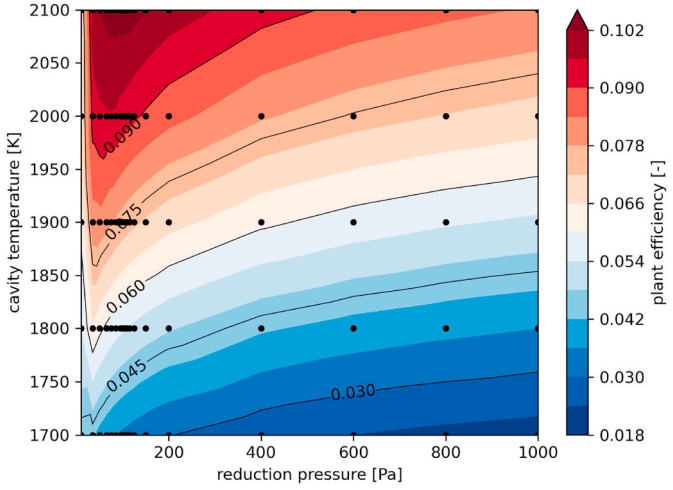

Fig. 12. Plant efficiency as function of the reduction pressure and the cavity temperature. The other four "free" parameters are selected individually at each data point such that the plant efficiency is optimized.

cavity temperatures. One reason for this phenomenon is that the reduction extent grows non-linearly with temperature and similarly the reduction energy fraction (Equation (18)) is monotonically increasing over the considered temperature range (see Fig. 3). Another important reason is the contribution of radiative heat transfer to the effective thermal conductivity within the RPC. The radiative contribution modelled by the Rosseland diffusion approximation increases with the cube of the temperature and is the dominant contributor to the effective thermal conductivity at the occurring temperatures. The upper temperature of 2100 K in this study seems quite high if compared to the state-of-the-art receiver-reactors which are often operated at a nominal temperature of about 1773 K. Here, it is important to note that even in the state-of-the-art systems the redox material is heated to temperatures significantly above this nominal temperature. This is because the nominal temperature in these experiments was measured at the back of the directly irradiated RPC and not at the front were the highest temperatures are reached [11]. In order to quantify the actual maximum temperatures, numerical models have been applied. Zoller et al. [48] derived simulated peak temperatures of more than 2100 K for the receiver-reactor developed in the project SUN-to-LIQUID when operated with 50 kW radiative input power. Thus, it is expected that peak temperatures close to 2100 K have already been reached in receiver-reactors during demonstration campaigns. Nevertheless, operating at such high temperatures has to be carefully assessed, since phase transitions [87], including melting and sublimation [6,88], have to be avoided. In addition, local degradation of the ceria RPCs during experimental campaigns has been reported, mainly attributed to induced cyclic stresses by thermal and chemical expansion [11]. Therefore, the elevated temperatures as well as the rapid transients might pose severe challenges for the applied materials. Redox material development efforts should address these challenges in addition to the general goal of identifying materials with more favorable thermodynamic and kinetic characteristics.

Another interesting aspect is the effect of the RMA radius on the plant efficiency as seen in Fig. 13. Compared to the receiver-reactor efficiency values in Fig. 9, in the plant level analysis, the peak is shifted to slightly lower concentration factors. Furthermore, the relative plant efficiency variations in Fig. 13 are much smaller than in Fig. 9. This is due to the use of recovered waste heat to compensate the vacuum pumping energy demand and probably foremost due to the optimal selection of the other four parameters. While Fig. 9 seemed to suggest that the RMA thickness is critical and limited to values below 0.02 m, when considering all combinations of the other parameters, sets of parameters can be identified even for large RMAs that lead to an overall plant efficiency close to the peak values. Still, the highest values are obtained at high concentration factors and small RMA radii in accordance to Fig. 10.

Smaller RMAs might pose implementation challenges since they are expected to have a lower mechanical stability and more importantly, smaller RMAs result in larger numbers of RMAs which need to be integrated into the receiver-reactor. They also reach the highest efficiencies at relatively small reduction step durations. Looking at the reduction duration as function of RMA radius and concentration factor reveals that the reduction durations in the region with the highest plant efficiencies (>10.2 %) are at below 300 s (see Fig. 14). This is expected to be a significant challenge for the material due to the necessary high heating rates.

A qualitative aspect of Fig. 14 worth mentioning is the quite irregular and fine structured contours compared to the plant efficiencies presented in the figures above. While all plots in this chapter where generated by optimizing the plant efficiency, Fig. 14 does not show the plant efficiency values as such, but the corresponding reduction durations. The reduction duration is a result of the plant simulation and dependents on the other four parameters which are not indicated in the plot. Therefore, each data point might have a different combination of

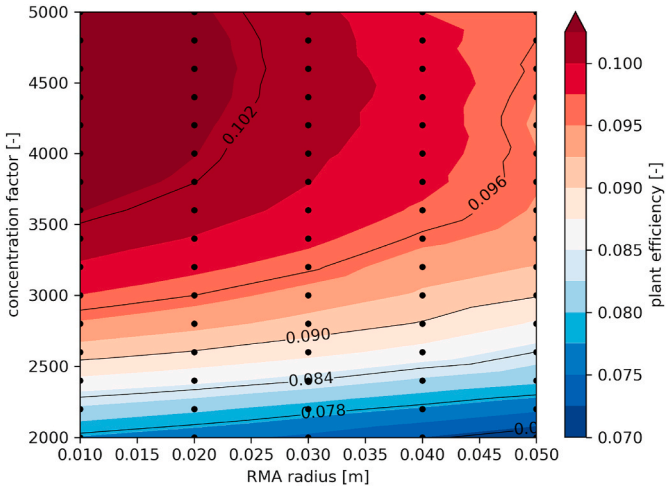

Fig. 13. Plant efficiency as function of the RMA radius and the concentration factor. The other four "free" parameters are selected individually at each data point such that the plant efficiency is optimized.

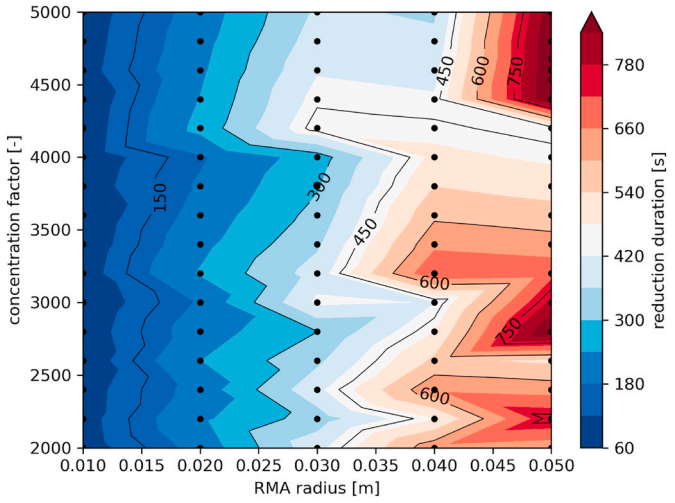

Fig. 14. Reduction duration as a function of RMA radius and concentration factor. The other four "free" parameters are selected individually for each data point so that the plant efficiency is optimized.

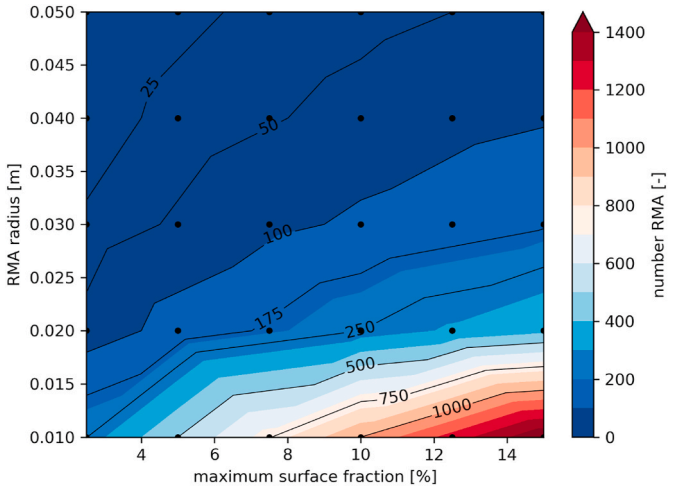

Fig. 15. Number of RMAs as a function of the maximum surface fraction and the RMA radius. The other four "free" parameters are selected individually for each data point so that the plant efficiency is optimized. The results show a large range for the number of applied RMAs with values below 25 to values above 1300.

the "free" parameters cavity temperature, reduction pressure, aperture radius and maximum surface fraction. In some areas one can expect, that the plant efficiencies are very close to each other for a number of parameter sets, and the reduction duration might react more strongly to changes in the "free" parameters. Therefore, a finer resolution of the parameters might resolve observable irregularities only to some extent.

As mentioned above, one technical challenge related to small RMAs is the high number of RMA units to be implement in the receiver-reactor. As seen in Fig. 15 for RMAs with a radius below 0.02 m several hundred up to more than 1300 RMAs need to be implemented. On the other side, for RMAs with a radius above 0.03 m the maximum number of RMAs drops below 175. This seems much more realistic, even though the numbers are still quite large. For RMAs with a radius of 0.05 m values below 50 RMAs can be observed, while high plant efficiencies of >9 % are still obtainable, indicating design flexibility. Similarly, it is expected that other parameters like the reduction time can be tailored to some extent, leading to reasonable compromises between technical feasibility and plant performance, once the technical and implementation challenges are understood in more detail.

While the presented study already resulted in attractive plant efficiency values within the ranges of the investigated parameters, only 6 of all of the model parameters have been varied so far and further optimization potential is to be expected when extending the analysis. In particular the effect of the oxidation conditions seems relevant and should be investigated in more detail. Additional optimization opportunities are expected if other redox materials are analyzed, or if plant modifications like the implementation of solid-solid heat recovery systems, volumetrically absorbing redox structures or alternative oxygen removal technologies (e.g. thermochemical oxygen pumps) are considered. Furthermore, 25%–30% of the total energy input is lost in the form of highly concentrated radiation or at high temperatures given by the waste fraction (see Equation (30)). It will be crucial for the overall plant efficiency and the economic competitiveness of the technology to make more effective use of these flows of energy, for example, by integrating the fuel production plant with other processes like direct air capture [89] or electricity production.

4. Conclusions

A new version of R2Mx with surrounding fields is introduced and a comprehensive plant model is presented. The receiver-reactor design comprises a large number of individually controllable, cylindrical redox structures and promotes the indirect heating of the RMAs. The largest receiver input power analyzed was 13.7 MW, with a corresponding solar field power of 26.6 MW. Such plant sizes showcase plants at relevant scale, knowing that for a large-scale mass production, this needs to be scaled-up even further. The scale-up approach of increasing the receiver-reactor size, the number of RMAs and the number of apertures is, up to a certain power level, rather straight forward. For ever larger plant sizes, the optical efficiency is expected to decrease, limiting the size of a single tower plant. Beyond this limit, multi-tower configurations might be the preferred solution.

The heating of a cylindrical redox structure in an indirectly irradiated environment, as in R2Mx, was simulated. A comparison to a plate-shaped redox material as in the directly irradiated receiver-reactors, representing the state-of-the-art systems, highlighted very interesting characteristics of the new version of R2Mx. The main benefit is the thermal distribution of the redox mass which is much more benign for the R2Mx case, where the largest values of the mass fraction distribution are at the highest temperatures and the temperature spread is relatively small. Another benefit is related to the maximum temperature of the redox material which is, in case of R2Mx, defined by the cavity temperature. In contrast, the maximum temperature in the directly irradiated case tends to increase to values beyond the tolerable limits of the applied materials, due to the necessary high concentration factors. Therefore, the reduction step in such systems is usually stopped "prematurely". These characteristics make a strong case for the R2Mx approach and its indirect heating of cylindrical redox structures.

Out of the investigated parameters, the overall plant performance depends most strongly on the cavity temperature and the reduction pressure. From a plant efficiency standpoint, higher temperatures are preferable even though heat losses of the receiver increase. The main reasons are the non-linear increase of reduction extent with temperature and the higher effective thermal conductivity of the open porous structures at elevated temperatures. Therefore, the optimal receiver-reactor operation temperature will most likely be limited rather by the physical and chemical stability of the redox structure and the other receiver-reactor materials and not by heat loss considerations.

Average annual plant efficiencies of up to 10.5 % for a 3.7 MW receiver-reactor have been obtained, which is already close to commercial solutions (PV + AEL) and the possibility to split water as well as CO_2 is a distinct advantage. Importantly, so far, about 28% of the total energy in the R2Mx plant is lost in the form of highly concentrated radiation or high temperature heat. If this high-quality energy resource

can be exploited more effectively, R2Mx has the potential to clearly outperform the commercial alternative. In addition, several of the underlying model assumptions are relatively conservative and promising modifications of the process have not yet been considered in the model. Therefore, it is anticipated that significant improvement opportunities can be exploited at subsequent stages development.

CRediT authorship contribution statement

Stefan Brendelberger: Writing – review & editing, Writing – original draft, Visualization, Validation, Project administration, Methodology, Investigation, Funding acquisition, Formal analysis, Data curation, Conceptualization.

Declaration of generative AI and AI-assisted technologies in the writing process

During the preparation of this work the author used DeepL in order to improve readability and language. After using this tool/service, the author reviewed and edited the content as needed and takes full responsibility for the content of the publication.

Declaration of competing interest

The authors declare the following financial interests/personal relationships which may be considered as potential competing interests: Stefan Brendelberger has patent Thermochemisches Reaktorsystem sowie Solaranlage mit thermochemischem Reaktorsystem issued to Deutsches Zentrum für Luft-und Raumfahrt e.V. If there are other authors, they declare that they have no known competing financial interests or personal relationships that could have appeared to influence the work reported in this paper.

Acknowledgement

This work was partially funded by the German Federal Ministry for Economic Affairs and Climate Action under the funding code Redox3D (03EE5124A). The author is responsible for the content of this publication.

References

[1] Nakamura T. Hydrogen production from water utilizing solar heat at high temperatures. Sol Energy 1977;19:467–75.
[2] Steinfeld A, Sanders S, Palumbo R. Design aspects of solar thermochemical engineering - a case study: two-step warer-splitting cycle using Fe$_3$O$_4$/FeO redox system. Sol Energy 1999;65:43–53. https://doi.org/10.1016/s0038-092x(98)00092-9.
[3] Kodama T. High-temperature solar chemistry for converting solar heat to chemical fuels. Prog Energy Combust Sci 2003;29:567–97.
[4] Muhich CL, Ehrhart BD, Al-Shankiti I, Ward BJ, Musgrave CB, Weimer AW. A review and perspective of efficient hydrogen generation via solar thermal water splitting. Wiley Interdisciplinary Reviews: Energy Environ 2016;5:261–87.
[5] Agrafiotis C, Roeb M, Sattler C. A review on solar thermal syngas production via redox pair-based water/carbon dioxide splitting thermochemical cycles. Renew Sustain Energy Rev 2015;42:254–85. https://doi.org/10.1016/j.rser.2014.09.039.
[6] Abanades S, Flamant G. Thermochemical hydrogen production from a two-step solar-driven water-splitting cycle based on cerium oxides. Sol Energy 2006;80:1611–23. https://doi.org/10.1016/j.solener.2005.12.005.
[7] de La Calle A, Bayon A. Annual performance of a thermochemical solar syngas production plant based on non-stoichiometric CeO2. Int J Hydrogen Energy 2019;44:1409–24. https://doi.org/10.1016/j.ijhydene.2018.11.076.
[8] Abanades S, Charvin P, Flamant G, Neveu P. Screening of water-splitting thermochemical cycles potentially attractive for hydrogen production by concentrated solar energy. Energy 2006;31:2805–22. https://doi.org/10.1016/j.energy.2005.11.002.
[9] Chueh WC, Haile SM. Ceria as a Thermochemical reaction medium for selectively generating syngas or methane from H_2O and CO_2. ChemSusChem 2009;2:735–9. https://doi.org/10.1002/cssc.200900138.
[10] Schäppi R, Rutz D, Dähler F, Muroyama A, Haueter P, Lilliestam J, Patt A, Furler P, Steinfeld A. Drop-in fuels from sunlight and air. Nature 2022;601:63–8. https://doi.org/10.1038/s41586-021-04174-y.
[11] Zoller S, Koepf E, Nizamian D, Stephan M, Patané A, Haueter P, Romero M, González-Aguilar J, Lieftink D, Wit ED, Brendelberger S, Sizmann A, Steinfeld A. A solar tower fuel plant for the thermochemical production of kerosene from H2O and CO2. Joule 2022;6:1606–16. https://doi.org/10.1016/j.joule.2022.06.012.
[12] Hoes M, Muhich CL, Jacot R, Patzke GR, Steinfeld A. Thermodynamics of paired charge-compensating doped ceria with superior redox performance for solar thermochemical splitting of H_2O and CO_2. J Mater Chem A 2017;5:19476–84. https://doi.org/10.1039/C7TA05824A.
[13] Lou J, Tian Z, Wu Y, Li X, Qian X, Haile SM, Hao Y. Thermodynamic assessment of nonstoichiometric oxides for solar thermochemical fuel production. Sol Energy 2022;241:504–14. https://doi.org/10.1016/j.solener.2022.05.008.
[14] Barcellos DR, Sanders MD, Tong J, McDaniel AH, O'Hayre RP. BaCe 0.25 Mn 0.75 O 3−δ —a promising perovskite-type oxide for solar thermochemical hydrogen production. Energy Environ Sci 2018;11:3256–65. https://doi.org/10.1039/C8EE01989D.
[15] Warren KJ, Tran JT, Weimer AW. A thermochemical study of iron aluminate-based materials: a preferred class for isothermal water splitting. Energy Environ Sci 2022;15:806–21. https://doi.org/10.1039/D1EE02679H.
[16] McDaniel AH, Miller EC, Arifin D, Ambrosini A, Coker EN, O'Hayre R, Chueh WC, Tong J. Sr-and Mn-doped $LaAlO_{3-\delta}$ for solar thermochemical H_2 and CO production. Energy Environ Sci 2013;6:2424–8.
[17] Miller JE, McDaniel AH, Allendorf MD. Considerations in the design of materials for solar-driven fuel production using metal-oxide thermochemical cycles. Adv Energy Mater 2014;4:1300469.
[18] Ezbiri M, Takacs M, Theiler D, Michalsky R, Steinfeld A. Tunable thermodynamic activity of La x Sr 1-x Mn y Al 1-y O 3-δ (0≤ x≤ 1, 0≤ y≤ 1) perovskites for solar thermochemical fuel synthesis. J Mater Chem A 2017.
[19] Jiang Q, Zhou G, Jiang Z, Li C. Thermochemical CO_2 splitting reaction with $Ce_xM_{1-x}O_{2-\delta}$ (M=Ti^{4+}, Sn^{4+}, Hf^{4+}, Zr^{4+}, La^{3+}, Y^{3+} and Sm^{3+}) solid solutions. Sol Energy 2014;99:55–66. https://doi.org/10.1016/j.solener.2013.10.021.
[20] Scheffe JR, McDaniel AH, Allendorf MD, Weimer AW. Kinetics and mechanism of solar-thermochemical H_2 production by oxidation of a cobalt ferrite–zirconia composite. Energy Environ Sci 2013:963–73.
[21] Muhich CL, Ehrhart BD, Witte VA, Miller SL, Coker EN, Musgrave CB, Weimer AW. Predicting the solar thermochemical water splitting ability and reaction mechanism of metal oxides: a case study of the hercynite family of water splitting cycles. Energy Environ Sci 2015;8:3687–99.
[22] Jarrett C, Chueh W, Yuan C, Kawajiri Y, Sandhage KH, Henry A. Critical limitations on the efficiency of two-step thermochemical cycles. Sol Energy 2016;123:57–73. https://doi.org/10.1016/j.solener.2015.09.036.
[23] Hoskins AL, Millican SL, Czernik CE, Alshankiti I, Netter JC, Wendelin TJ, Musgrave CB, Weimer AW. Continuous on-sun solar thermochemical hydrogen production via an isothermal redox cycle. Appl Energy 2019;249:368–76. https://doi.org/10.1016/j.apenergy.2019.04.169.
[24] Muhich CL, Blaser S, Hoes MC, Steinfeld A. Comparing the solar-to-fuel energy conversion efficiency of ceria and perovskite based thermochemical redox cycles for splitting H_2O and CO_2. Int J Hydrogen Energy 2018;43:18814–31.
[25] Venstrom LJ, de Smith RM, Hao Y, Haile SM, Davidson JH. Efficient splitting of CO_2 in an isothermal redox cycle based on ceria. Energy Fuels 2014;28:2732–42.
[26] Tran JT, Warren KJ, Mejic D, Anderson RL, Jones L, Hauschulz DS, Wilson C, Weimer AW. Pressure-enhanced performance of metal oxides for thermochemical water and carbon dioxide splitting. Joule 2023;7:1759–68. https://doi.org/10.1016/j.joule.2023.07.016.
[27] Ermanoski I, Miller JE, Allendorf MD. Efficiency maximization in solar-thermochemical fuel production: challenging the concept of isothermal water splitting. Phys Chem Chem Phys 2014;16:8418–27.
[28] Yuan C, Jarrett C, Chueh W, Kawajiri Y, Henry A. A new solar fuels reactor concept based on a liquid metal heat transfer fluid: reactor design and efficiency estimation. Sol Energy 2015;122:547–61.
[29] Brendelberger S, Sattler C. Concept analysis of an indirect particle-based redox process for solar-driven H2O/CO2 splitting. Sol Energy 2015;113:158–70. https://doi.org/10.1016/j.solener.2014.12.035.
[30] Brendelberger S, von Storch H, Bulfin B, Sattler C. Vacuum pumping options for application in solar thermochemical redox cycles – assessment of mechanical-, jet- and thermochemical pumping systems. Sol Energy 2017;141:91–102. https://doi.org/10.1016/j.solener.2016.11.023.
[31] Xu M, Ermanoski I, Stechel EB. Deng, shuguang %J chemical engineering journal. Oxygen pumping characteristics of $YBaCo4O_{7+\delta}$ for solar thermochemical cycles. 2020, 124026.
[32] Patankar AS, Wu X-Y, Choi W, Tuller HL, Ghoniem AF. A comparative analysis of integrating thermochemical oxygen pumping in water-splitting redox cycles for hydrogen production. Sol Energy 2023;264:111960. https://doi.org/10.1016/j.solener.2023.111960.
[33] Lin M, Haussener S. Solar fuel processing efficiency for ceria redox cycling using alternative oxygen partial pressure reduction methods. Energy 2015;88:667–79. https://doi.org/10.1016/j.energy.2015.06.006.
[34] Ehrhart BD, Muhich CL, Al-Shankiti I, Weimer AW. System efficiency for two-step metal oxide solar thermochemical hydrogen production – Part 3: various methods for achieving low oxygen partial pressures in the reduction reaction. Int J Hydrogen Energy 2016;41:19904–14. https://doi.org/10.1016/j.ijhydene.2016.07.106.
[35] Bai W, Huang H, Suter C, Haussener S, Lin M. Enhanced solar-to-fuel efficiency of ceria-based thermochemical cycles via integrated electrochemical oxygen pumping. ACS Energy Lett 2022;7:2711–6. https://doi.org/10.1021/acsenergylett.2c01318.

[36] Ermanoski I, Grobbel J, Singh A, Lapp J, Brendelberger S, Roeb M, Sattler C, Whaley J, McDaniel A, Siegel NP. Design and construction of a cascading pressure reactor prototype for solar-thermochemical hydrogen production. AIP Conf Proc 2016;1734:120001. https://doi.org/10.1063/1.4949203.
[37] Pullar RC, Novais RM, Caetano APF, Barreiros MA, Abanades S, Oliveira FAC. A review of solar thermochemical CO2 splitting using ceria-based ceramics with designed morphologies and microstructures. Front Chem 2019;7:601. https://doi.org/10.3389/fchem.2019.00601.
[38] Venstrom LJ, Petkovich N, Rudisill S, Stein A, Davidson JH. The effects of morphology on the oxidation of ceria by water and carbon dioxide. J Sol Energy Eng 2012;134:11005.
[39] Ben-Arfa BAE, Abanades S, Salvado IMM, Ferreira JMF, Pullar RC. Robocasting of 3D printed and sintered ceria scaffold structures with hierarchical porosity for solar thermochemical fuel production from the splitting of CO2. Nanoscale 2022;14:4994–5001. https://doi.org/10.1039/D2NR00393G.
[40] Hoes M, Ackermann S, Theiler D, Furler P, Steinfeld A. Additive-manufactured ordered porous structures made of ceria for concentrating solar applications. Energy Technol 2019;7. https://doi.org/10.1002/Ente.201900484.
[41] Eltayeb A, Graß V, Lee K, Pein M, Agrafiotis C, Schmücker M, Roeb M, Sattler C. Characterisation and thermochemical stability analysis of 3D printed porous ceria structures fabricated via composite extrusion Modelling. Mater Des 2023;236:112514. https://doi.org/10.1016/j.matdes.2023.112514.
[42] Sas Brunser S, Bargardi FL, Libanori R, Kaufmann N, Braun H, Steinfeld A, Studart AR. Solar-Driven redox splitting of CO 2 using 3D-printed hierarchically channeled ceria structures. Adv Mater Interfac 2023;10:2300452. https://doi.org/10.1002/admi.202300452.
[43] Lu Y, Zhu L, Agrafiotis C, Vieten J, Roeb M, Sattler C. Solar fuels production: two-step thermochemical cycles with cerium-based oxides. Prog Energy Combust Sci 2019;75:100785. https://doi.org/10.1016/j.pecs.2019.100785.
[44] Furler P, Scheffe J, Gorbar M, Moes L, Vogt U, Steinfeld A. Solar thermochemical CO_2 splitting utilizing a reticulated porous ceria redox system. Energy Fuel 2012;26:7051–9. https://doi.org/10.1021/ef3013757.
[45] Koepf E, Zoller S, Luque S, Thelen M, Brendelberger S, González-Aguilar J, Romero M, Steinfeld A. Liquid fuels from concentrated sunlight: an overview on development and integration of a 50 kW solar thermochemical reactor and high concentration solar field for the SUN-to-LIQUID project. AIP Conf Proc 2019;2126:180012. https://doi.org/10.1063/1.5117692.
[46] Marxer D, Furler P, Takacs M, Steinfeld A. Solar thermochemical splitting of CO_2 into separate streams of CO and O_2 with high selectivity, stability, conversion, and efficiency. Energy Environ Sci 2017;10:1142–9.
[47] Brendelberger S, Holzemer-Zerhusen P, Storch Hv, Sattler C. Performance assessment of a heat recovery system for monolithic receiver-reactors. J Sol Energ-T Asme 2019;141. https://doi.org/10.1115/1.4042241.
[48] Zoller S, Koepf E, Roos P, Steinfeld A. Heat transfer model of a 50 kW solar receiver–reactor for thermochemical redox cycling using cerium dioxide. J Sol Energ-T Asme 2019;141:21014.
[49] Diver RB, Miller JE, Siegel NP, Moss TA. Testing of a CR5 solar thermochemical heat engine prototype, ASME 2010 4th. International Conference on Energy Sustainability 2010;2:97–104.
[50] Lapp J, Davidson JH, Lipiński W. Heat transfer analysis of a solid-solid heat recuperation system for solar-driven nonstoichiometric redox cycles. J Sol Energ-T Asme 2013;135:31004. https://doi.org/10.1115/1.4023357.
[51] Patankar AS, Wu X-Y, Choi W, Tuller HL, Ghoniem AF. Efficient solar thermochemical hydrogen production in a reactor train system with thermochemical oxygen removal. In: Volume 6: energy, columbus, Ohio, USA. American Society of Mechanical Engineers; 2022.
[52] Weber A, Grobbel J, Neises-von Puttkamer M, Sattler C. Swept open moving particle reactor including heat recovery for solar thermochemical fuel production. Sol Energy 2023;266:112178. https://doi.org/10.1016/j.solener.2023.112178.
[53] Brendelberger S, Holzemer-Zerhusen P, Vega Puga E, Roeb M, Sattler C. Study of a new receiver-reactor cavity system with multiple mobile redox units for solar thermochemical water splitting. Sol Energy 2022;235:118–28. https://doi.org/10.1016/j.solener.2022.02.013.
[54] Kyrimis S, Le Clercq P, Brendelberger S. 3D modelling of a solar thermochemical reactor for MW scaling-up studies. AIP Conf Proc 2019;2126:180013. https://doi.org/10.1063/1.5117693.
[55] Groehn AJ, Lewandowski A, Yang R, Weimer AW. Hybrid radiation modeling for multi-phase solar-thermal reactor systems operated at high-temperature. Sol Energy 2016;140:130–40.
[56] Budama VK, Brendelberger S, Roeb M, Sattler C. Performance analysis and optimization of solar thermochemical water-splitting cycle with single and multiple receivers. Energ Tech 2022;10:2100220. https://doi.org/10.1002/ente.202100220.
[57] Ermanoski I, Siegel NP, Stechel EB. A new reactor concept for efficient solar-thermochemical fuel production. J Sol Energ-T Asme 2013;135:31002. https://doi.org/10.1115/1.4023356.
[58] Yang S, Li L, Wang B, Li S, Wang J, Lund P, Lipiński W. Thermodynamic analysis of a conceptual fixed-bed solar thermochemical cavity receiver–reactor array for water splitting via ceria redox cycling. Front Energy Res 2021;9:565761. https://doi.org/10.3389/fenrg.2021.565761.
[59] Ehrhart BD, Muhich CL, Al-Shankiti I, Weimer AW. System efficiency for two-step metal oxide solar thermochemical hydrogen production – Part 1: thermodynamic model and impact of oxidation kinetics. Int J Hydrogen Energy 2016;41:19881–93. https://doi.org/10.1016/j.ijhydene.2016.07.109.
[60] Moretti C, Patil V, Falter C, Geissbühler L, Patt A, Steinfeld A. Technical, economic and environmental analysis of solar thermochemical production of drop-in fuels. Sci Total Environ 2023;901:166005. https://doi.org/10.1016/j.scitotenv.2023.166005.
[61] Falter C, Scharfenberg N, Habersetzer A. Geographical potential of solar thermochemical jet fuel production. Energies 2020;13:802. https://doi.org/10.3390/en13040802.
[62] Schmitz M, Schwarzbözl P, Buck R, Pitz-Paal R. Assessment of the potential improvement due to multiple apertures in central receiver systems with secondary concentrators. Sol Energy 2006;80:111–20. https://doi.org/10.1016/j.solener.2005.02.012.
[63] Martinek J, Channel M, Lewandowski A, Weimer AW. Considerations for the design of solar-thermal chemical processes. J Sol Energy Eng 2010;132. 031013-1 - 031013-6.
[64] Boretti A, Castelletto S, Al-Zubaidy S. Concentrating solar power tower technology: present status and outlook. Nonlinear Eng 2019;8:10–31. https://doi.org/10.1515/nleng-2017-0171.
[65] Pitz-Paal R, Botero NB, Steinfeld A. Heliostat field layout optimization for high-temperature solar thermochemical processing. Sol Energy 2011;85:334–43.
[66] Martinek J, Viger R, Weimer AW. Transient simulation of a tubular packed bed solar receiver for hydrogen generation via metal oxide thermochemical cycles. Sol Energy 2014;105:613–31. https://doi.org/10.1016/j.solener.2014.04.022.
[67] Ackermann S, Steinfeld A. Spectral hemispherical reflectivity of nonstoichiometric cerium dioxide. Sol Energy Mater Sol Cell 2017;159:167–71. https://doi.org/10.1016/j.solmat.2016.08.036.
[68] Ackermann S, Takacs M, Scheffe J, Steinfeld A. Reticulated porous ceria undergoing thermochemical reduction with high-flux irradiation. Int J Heat Mass Tran 2017;107:439–49.
[69] Bulfin B, Call F, Lange M, Lübben O, Sattler C, Pitz-Paal R, Shvets IV. Thermodynamics of CeO2 thermochemical fuel production. Energy Fuel 2015;29:1001–9. https://doi.org/10.1021/ef5019912.
[70] Ermanoski I. Maximizing efficiency in two-step solar-thermochemical fuel production, international conference on concentrating solar power and chemical energy systems. SolarPACES 2014;69:1731–40. https://doi.org/10.1016/j.egypro.2015.03.141. 2015.
[71] Li S, Wheeler VM, Kreider PB, Lipiński W. Thermodynamic analyses of fuel production via solar-driven non-stoichiometric metal oxide redox cycling. Part 1. Revisiting flow and equilibrium assumptions. Energy Fuel 2018;32:10838–47. https://doi.org/10.1021/acs.energyfuels.8b02081.
[72] Li S, Wheeler VM, Kumar A, Venkataraman MB, Muhich CL, Hao Y, Lipiński W. Thermodynamic guiding principles for designing nonstoichiometric redox materials for solar thermochemical fuel production: ceria, perovskites, and beyond. Energy Tech 2022;10:2000925. https://doi.org/10.1002/ente.202000925.
[73] Cheng W-H, de La Calle A, Atwater HA, Stechel EB, Xiang C. Hydrogen from sunlight and water: a side-by-side comparison between photoelectrochemical and solar thermochemical water-splitting. ACS Energy Lett 2021;6:3096–113. https://doi.org/10.1021/acsenergylett.1c00758.
[74] Hathaway BJ, Bala Chandran R, Gladen AC, Chase TR, Davidson JH. Demonstration of a solar reactor for carbon dioxide splitting via the isothermal ceria redox cycle and practical implications. Energy Fuel 2016;30:6654–61.
[75] Brendelberger S, Rosenstiel A, Lopez-Roman A, Prieto C, Sattler C. Performance analysis of operational strategies for monolithic receiver-reactor arrays in solar thermochemical hydrogen production plants. Int J Hydrogen Energy 2020;45:26104–16. https://doi.org/10.1016/j.ijhydene.2020.06.191.
[76] VDI heat atlas. second ed. Berlin, Heidelberg: Springer-Verlag; 2010.
[77] Riess I, Ricken M, Nölting J. On the specific heat of nonstoichiometric ceria. J. Solid State Chem., J. Solid State Chem. 1985;57:314–22. https://doi.org/10.1016/0022-4596(85)90193-8.
[78] Grobbel J. Modellierung von solaren Partikelreceivern mit der Diskreten Elemente Methode. 2019.
[79] Vega Puga E, Brendelberger S, Weber A, Sattler C. Modelling development of a receiver-reactor of type R2Mx for thermochemical water splitting. In: ASME 2023 17th international conference on energy sustainability. Washington, DC, USA: American Society of Mechanical Engineers; 2023.
[80] Panlener RJ, Blumenthal RN, Garnier JE. A thermodynamic study of nonstoichiometric cerium dioxide. J Phys Chem Solid 1975;36:1213–22. https://doi.org/10.1016/0022-3697(75)90192-4.
[81] Patankar SV. Numerical heat transfer and fluid flow. CRC Press; 2018.
[82] Thanda VK, Fend T, Laaber D, Lidor A, Storch Hv, Säck JP, Hertel J, Lampe J, Menz S, Piesche G, Berger S, Lorentzou S, Syrigou M, Denk T, Gonzales-Pardo A, Vidal A, Roeb M, Sattler C. Experimental investigation of the applicability of a 250 kW ceria receiver/reactor for solar thermochemical hydrogen generation. Renew Energy 2022;198:389–98. https://doi.org/10.1016/j.renene.2022.08.010.
[83] Brendelberger S. Results from a solar thermochemical plant model of type R2Mx for hydrogen production at MW scale. Zenodo 2024. v1, https://doi.org/10.5281/zenodo.13929803.
[84] Menz S, Lampe J, Krause J, Seeger T, Fend T. Holistic energy flow analysis of a solar driven thermo-chemical reactor set-up for sustainable hydrogen production. Renew Energy 2022;189:1358–74. https://doi.org/10.1016/j.renene.2022.03.033.
[85] Oberkirsch L, Grobbel J, Maldonado Quinto D, Schwarzbözl P, Hoffschmidt B. Controlling a solar receiver with multiple thermochemical reactors for hydrogen

production by an LSTM neural network based cascade controller. Sol Energy 2022; 243:483–93. https://doi.org/10.1016/j.solener.2022.08.007.
[86] Siegel NP, Miller JE, Ermanoski I, Diver RB, Stechel EB. Factors affecting the efficiency of solar driven metal oxide thermochemical cycles. Ind Eng Chem Res 2013;52:3276–86. https://doi.org/10.1021/ie400193q.
[87] Zinkevich M, Djurovic D, Aldinger F. Thermodynamic modelling of the cerium–oxygen system. Solid State Ionics 2006;177:989–1001. https://doi.org/10.1016/j.ssi.2006.02.044.
[88] Roine A. Outokumpu HSC chemistry for windows: chemical reaction and equilibrium software with extensive thermochemical database, User's guide. 2002. version 5.
[89] Prats-Salvado E, Monnerie N, Sattler C. Techno-economic assessment of the integration of direct air capture and the production of solar fuels. Energies 2022; 15:5017. https://doi.org/10.3390/en15145017.